Mon. Not. R. Astron. Soc. **342,** 995–1008 (2003)

The structure of the narrow-line region in Cygnus A

M. D. Taylor,★ C. N. Tadhunter and T. G. Robinson
Department of Physics and Astronomy, University of Sheffield, Sheffield S3 7RH

Accepted 2003 March 7. Received 2003 March 7; in original form 2003 January 20

ABSTRACT

We present intermediate-resolution spectra for the powerful radio galaxy Cygnus A taken with the ISIS spectrograph on the William Herschel Telescope. The spectra show complex emission-line profiles across the entire extent of the narrow-line region (NLR) along the radio axis (PA 105°), with line splittings ($\Delta\ V \sim 300$ km s^{-1}) at radial distances of 1–2 kpc to both the north-east and south-west, and a combination of broad ($500 <$ FWHM < 800 km s^{-1}) and narrow (FWHM < 300 km s^{-1}) components within a radial distance of 1 kpc of the nucleus. The wide spectral coverage of the data allows us for the first time to measure the reddening, physical conditions and ionization of the kinematic subcomponents individually. Only the broad component detected in the near-nuclear regions shows evidence for significant reddening over and above that due to the Galaxy. The level of reddening of the nuclear broad component is consistent with the idea that the extinction associated with the kiloparsec-scale dust lane induces a mild ($\leqslant$factor 2) anisotropy in the total emission-line flux, although there is no evidence for a compact, high-density inner narrow-line region in this source. Following correction for reddening, we find a remarkable degree of uniformity in the physical conditions and ionization state between the various spatial and kinematic subcomponents, suggesting a common ionization mechanism for all the subcomponents, despite the differences in kinematics. We use diagnostic diagrams to demonstrate that photoionization by the active galactic nucleus is the dominant ionization mechanism. However, a combination of matter- and radiation-bounded photoionized components is required to explain the strength of the [Fe VII] λ6087 line and the high electron temperature measured from the [O III] $(5007 + 4959)/4363$ diagnostic ratio. A major outstanding issue for our understanding of the NLR gas in this and other radio galaxies is how the uniformity in the ionization and physical conditions can be maintained in a mixed photoionized medium across a range of spatial scales and kinematic subcomponents.

Key words: line: formation – galaxies: active – galaxies: individual: Cygnus A – galaxies: nuclei.

1 INTRODUCTION

The kiloparsec-scale narrow-line region (NLR) is the brightest and easiest to study spectral component detected in powerful radio galaxies. It is important for helping us to develop our understanding of radio galaxies for several reasons. First, an understanding of the dominant ionization mechanism for the NLR is crucial for interpretation of the now well-established correlations between radio power and the narrow emission-line luminosity, which can provide key information about the nature of energy generation mechanisms in active galactic nuclei (AGN) (Rawlings & Saunders 1991). Secondly, comparisons between the NLR properties of radio galaxies and quasars provide a means of testing the anisotropy-based unified schemes for powerful radio sources (Barthel 1989). Finally, investigations into the kinematics of the NLR gas can be used to gauge the impact of the jet and quasar activity on the interstellar medium (ISM) of the host galaxies, and search for evidence for supermassive black holes.

Given the importance of the NLR in radio galaxies, it is surprising that, while there have been a large number of observations and studies of the NLR in Seyfert galaxies (e.g. de Robertis & Osterbrock 1984, 1986; Pelat, Alloin & Fosbury 1981), there have been few comparable studies of the warm gas on a $\sim$1 kpc scale in powerful radio galaxies. The work that has been undertaken for radio galaxies has involved high-resolution single-aperture spectroscopy of the NLR (Heckman, Miley & Green 1984; Brotherton 1996), concentrating on the profiles of single emission lines (usually [O III]). Moreover, although a considerable amount of work has been done on investigating the

★E-mail: m.d.taylor@sheffield.ac.uk

ionization and kinematics of the warm gas in the larger-scale extended emission-line region (EELR: $r \sim 5$–100 kpc), almost no similar work has been carried out on the near-nuclear NLR.

There are a number of key issues that have yet to be resolved for the NLR of powerful radio galaxies:

(i) **The inner narrow-line region (INLR).** Is there a region of high density, high velocity dispersion and high ionization state close to the nucleus (<100 pc)? This is important for two reasons. First, the high densities and density stratification of the putative INLR would affect our ability to interpret the emission-line spectra of the nuclear regions. Secondly, the existence of an INLR would help to reconcile the unified schemes for powerful radio galaxies with the observed differences between the [O III] λ5007 and [O II] λ3727 luminosities of quasars and radio galaxies (Jackson & Browne 1990; Hes, Barthel & Fosbury 1993).

(ii) **Ionization mechanisms.** On the scale of the EELR (>5 kpc), there is clear kinematic and ionization evidence for a mixture of ionization mechanisms (Tadhunter 2002), with jet-induced shocks dominating in some objects (Villar-Martín et al. 1998; Clark et al. 1998). It is often assumed that the NLR (<1 kpc) is predominantly photoionized by the AGN, but there is little direct evidence to support this.

(iii) **Origin of the gas motions.** For Seyfert galaxies, the blue asymmetries measured in the broad wings of the forbidden lines (Heckman et al. 1981) are suggestive of radial flows, possibly AGN-induced outflows, while the correlations between the forbidden-line widths and the host galaxy bulge luminosities indicate that the linewidths reflect the gravitational potentials in the cores of the galaxies (Whittle 1992). However, in part as a result of the paucity of information, the situation is far less clear for powerful radio galaxies (e.g. compare Heckman et al. 1984 with Brotherton 1996); there is considerable uncertainty about the nature of their near-nuclear emission-line kinematics and what these might reveal about the impact of the activity on the ISM in the host galaxies.

In order to resolve these issues, spatially resolved line profile observations for a large number of emission-line species are required for individual radio galaxies. As the most powerful radio source in the local universe, Cygnus A ($z = 0.056$) is an ideal object for such studies. The close proximity of this source allows for detailed, spatially resolved studies of the optical spectrum on a 1 kpc scale. The emission lines in Cygnus A also have a relatively large equivalent width as a consequence of the heavily extinguished optical continuum (Osterbrock & Miller 1975).

Previous imaging, kinematic and polarimetric observations of Cygnus A reveal considerable complexity in its NLR, but also important clues to the dominant physical mechanisms.

Polarimetric studies by Tadhunter, Scarrott & Rolph (1990) and Ogle et al. (1997) provide direct evidence that the NLR in Cygnus A is illuminated by an AGN hidden from our direction at optical wavelengths by dust obscuration. Further evidence for anisotropic illumination is provided by high-resolution *HST* emission-line images, which show the existence of broad ionization cones on a 1–2 kpc scale (Jackson et al. 1996).

However, despite the compelling evidence for AGN illumination, there is also strong evidence for the effects of jet–cloud interactions and AGN-induced outflows in the NLR gas. Most notably, high-velocity emission-line components (Tadhunter 1991) and line splitting (Stockton, Ridgway & Lilly 1994) are detected in the north-west cone, and emission-line images show evidence for channels of lower emission-line flux where the jet passes through the north-west emission-line regions (Jackson et al. 1996). Moreover, the near-infrared detection of edge-brightened biconical structures close to the central point source (<0.5 kpc) provides further evidence for the effects of circumnuclear outflows (Tadhunter et al. 1999).

In addition to the emission-line cones on a ∼1 kpc scale to the north-west (NW) and south-east (SE), high-resolution *HST* emission-line images show evidence for a compact, high surface brightness structure close to the radio core (Jackson, Tadhunter & Sparks 1998). Evidence has also been found for an increase in the widths of the [O III] λ5007 emission lines towards the nucleus (Tadhunter, Metz & Robinson 1994). Both of these features may be consistent with presence of an INLR in Cygnus A.

Although it is clear that a mixture of mechanisms is required in order to understand the complex structures and kinematics of Cygnus A, the relative importance of the physical mechanisms remains unclear. In this paper we attempt to resolve the key issues surrounding the nature of the NLR in Cygnus A, using high-quality, intermediate-resolution, long-slit spectra taken using the ISIS spectrograph on the William Herschel Telescope (WHT). These data utilize the unique ability of ISIS to cover a large wavelength range at intermediate spectral resolution, thus enabling investigation of the kinematics, reddening and ionization of a range of important diagnostic emission lines simultaneously.

We assume the cosmological parameters $H_0 = 75$ km s^{-1} Mpc^{-1} and $q_0 = 0.0$ throughout this paper. For these parameters 1.00 arcsec corresponds to 1.00 kpc at the redshift of Cygnus A.

2 OBSERVATIONS

The observations were made in 1999 July using the ISIS spectrograph on the 4.2-m WHT on La Palma. Three sets of 1800-s exposures were taken simultaneously on each of the red and blue arms of ISIS, with a wavelength range of 3818–5378 Å on the blue arm, and 6034–7560 Å on the red. The EEV12 chip with the R600B grating was used on the blue arm, and on the red arm, the TEK4 chip was used with the R316R grating.

The seeing, measured by fitting the spatial profiles of stars along the slit, was found to be 0.97 ± 0.01 arcsec (full width at half-maximum, FWHM) in the co-added blue spectrum and 0.84 ± 0.03 arcsec (FWHM) in the co-added red. The airmass during the observations varied between 1.027 and 1.095, ensuring that the effects of differential atmospheric refraction were minimized. The slit was aligned along the radio axis (PA 105°) and a slit width of 1.32 arcsec was used throughout the observations. The spectral resolution, measured by fitting Gaussians to the night sky lines, was found to be 2.20 ± 0.07 Å in the blue spectrum and 3.93 ± 0.04 Å in the red.

The data were reduced using both the Starlink FIGARO package and IRAF. The bias was first subtracted and then the cosmic rays removed. The majority of the cosmic rays were removed using the IMCOMBINE routine with the median option in IRAF, after checking for any shifts between the frames and correcting for them. Any remaining cosmic rays were then removed by hand using IMEDIT. The data were then wavelength-calibrated, corrected for atmospheric extinction and flux-calibrated using the arc exposures and standard stars that were taken at the same time as the Cygnus A spectra. Based on the measurement of night sky emission lines, the wavelength calibration was found to be accurate to within ±0.1 Å in the co-added blue spectrum and to within ±0.2 Å in the co-added red spectrum. The data were also corrected for any residual spatial distortions and tilt by using the spectra of stars that lay along the slit. After correction, the residual offset in the spatial direction between the two ends of the spectra was estimated to be <0.1 pixel. The red

composite image was resampled to give the same spatial pixel scale as the blue image (0.2 arcsec pixel^{-1}). The two composite images were then spatially aligned and shifted back to the rest frame using the mean redshift calculated from the brighter emission lines ($z = 0.055\,683$). We estimate a relative flux calibration error of ± 5 per cent across the spectral range of the observations.

Finally, the emission-line data were analysed using the DIPSO package, which allows multiple Gaussian profiles to be fitted to the emission lines.

3 RESULTS

Grey-scale representations of the red and blue long-slit spectra in the region of [O III] λλ4959,5007 and Hα/[N II] are shown in Fig. 1. It is immediately clear from this figure that the line profiles are highly structured across the full extent of the emission-line nebula. In particular, a broad component is visible at the position of the radio core and there is evidence for line splitting in the NW and SE extended regions.

In the following sections we will present results based on row-by-row analysis of the bright [O III] λλ5007,4959 emission lines, and also more detailed analysis of the emission-line profiles and line ratios in subregions across the nebula. The apertures used for the latter analysis are shown in Fig. 2. Aperture B is coincident with the high surface brightness emission-line structure visible in *HST* images at the location of the radio core (Jackson et al. 1998); aperture A corresponds to the bright NW emission-line region; while apertures C and D cover the SE emission-line region.

3.1 Linewidths and correlations

Spectroscopic studies have demonstrated that the ionization potential and/or critical density of the emission lines is correlated with the linewidth (FWHM) in many Seyfert galaxies (de Robertis & Osterbrock 1984, 1986). Such studies – which provide evidence for density stratification in the NLR – have not previously been undertaken for powerful radio galaxies. Cygnus A is an obvious candidate to look for such correlations owing to its unique status as a powerful radio galaxy at low redshift with strong emission lines. Moreover, there is clear evidence for broad emission-line components at the location of its radio core (see Fig. 1).

For reference, the summed one-dimensional red and blue spectra from aperture B, the nuclear region, are shown in Fig. 3.

Initially, single Gaussians were freely fitted to all the detectable emission lines in the red and blue spectra and the widths quadratically corrected for instrumental broadening using the measured widths of the night sky lines. Table 1 shows the results of these fits, listing the line identification and the width of each line (FWHM). We identify no new features; however, compared with Tadhunter et al. (1994) and Thornton, Stockton & Ridgway (1999), we make more secure identification of the [Ar IV] λ4711, [Ar IV] λ4740 and [Ar V] λ7006 lines.

These single-Gaussian free fits allowed us to study the possibility of correlations between the ionization potential or critical density and linewidth (FWHM). We use these fits as they are a complete set of freely fitted Gaussians, something that is not always possible when using double-Gaussian fits (see Section 3.2). Fig. 4 presents

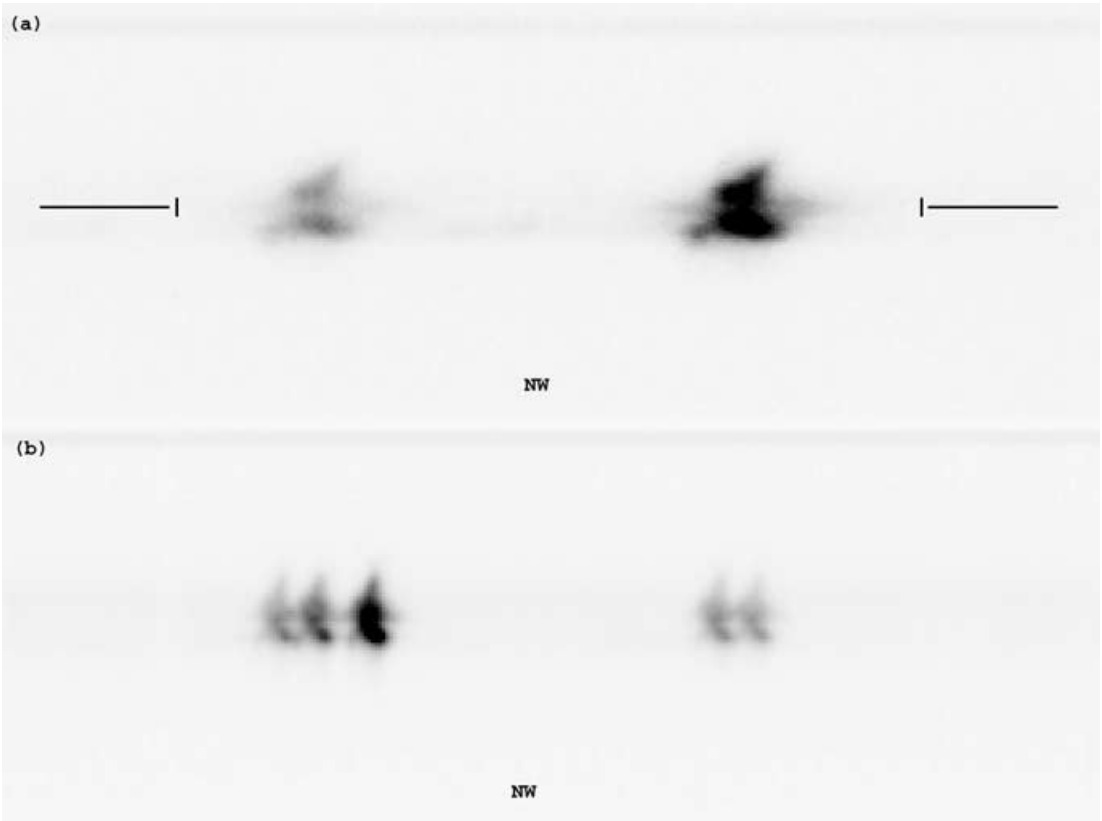

Figure 1. (a) The 2D spectrum for the [O III] λλ4959, 5007 lines from the blue spectrum; and (b) the [N II] λ6548/Hα/[N II] λ6584 and [S II] λλ6717, 6731 lines from the red spectrum. The PA of the observations was 105°, coincident with the radio axis. The horizontal lines on the blue image represent the centre of the radio core and the vertical lines 1 arcsec.

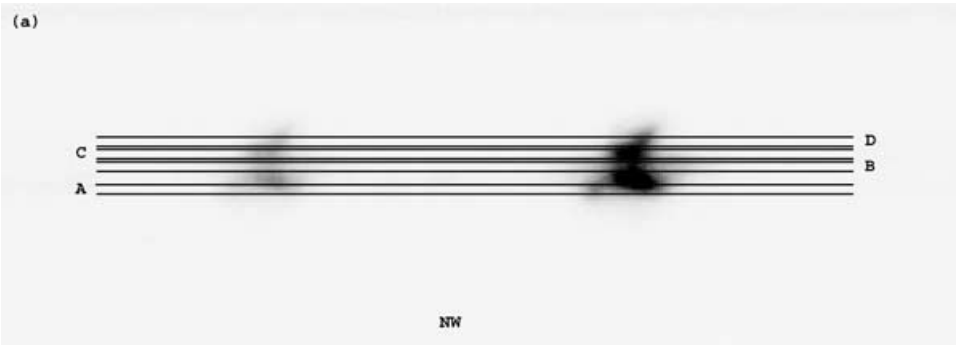

Figure 2. The apertures used in the detailed study of Cygnus A, as described below, overlaid on the [O III] λλ4959, 5007 lines. The four apertures represent the following regions: A = −2.0 → −1.2 arcsec, B = −0.4 → 0.4 arcsec, C = 0.4 → 1.2 arcsec and D = 1.2 → 2.0 arcsec from the central position.

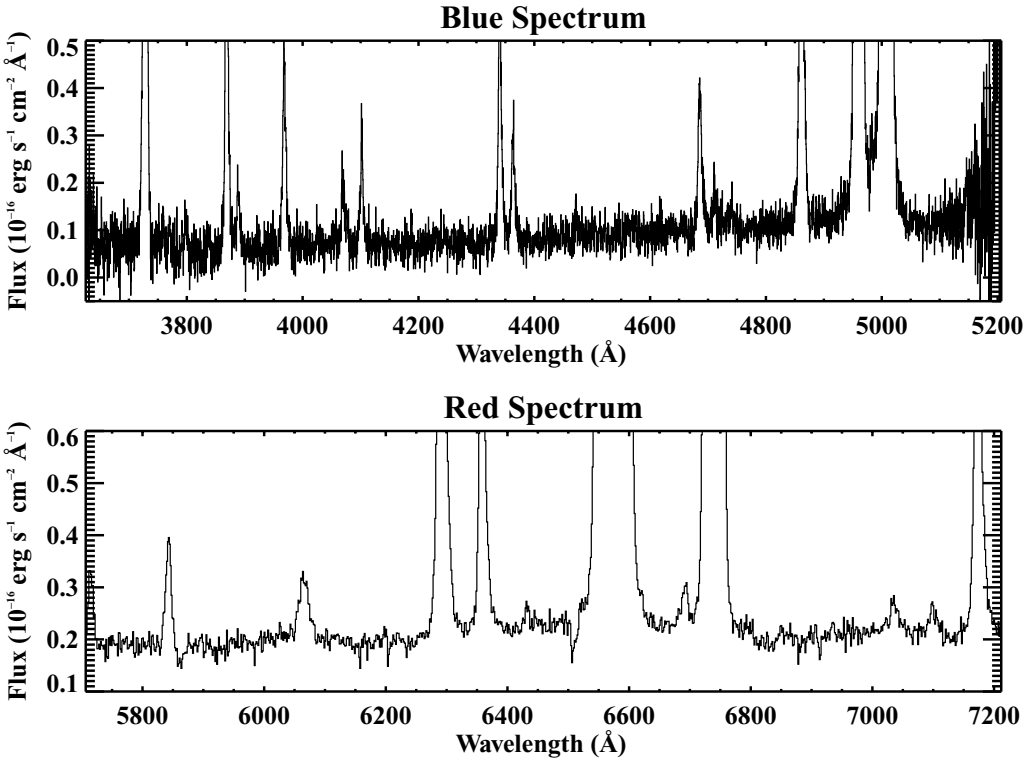

Figure 3. One-dimensional summed red and blue spectra extracted from aperture B.

a plot of ionization potential versus FWHM for aperture B (the nucleus).

Using the Pearson product moment correlation coefficient, we find no evidence for a significant correlation between ionization potential and FWHM, or between critical density and FWHM, in any of the apertures, certainly not at the level of significance seen in Seyfert galaxies (de Robertis & Osterbrock 1984, 1986). The correlation coefficient ranges between 0.006 and 0.345 for the 26–28 lines measured. However, the [Fe VII] λ6086 line is significantly broader than the other lines in apertures A, B and C. This is clear from cursory inspection of Fig. 3 and Table 1.

The single-Gaussian fits highlight the complex nature of the emission-line profiles. The left-hand plots in Fig. 5 show that single-Gaussian fits to the [O III] λ5007, Hβ and [O I] λ6300 lines fail to provide a good fit in the wings of the lines.

3.2 Double-Gaussian [O III] fits

The [O III] λ5007 line is the brightest in the spectrum of Cygnus A and, as we have seen in Section 3.1, has a complex line profile that a single Gaussian is unable to model. The next most sophisticated model is to use two Gaussians to fit the emission-line profile. Note that double Gaussians have been successfully used to model the emission lines in the EELR of radio galaxies with strong jet–cloud interactions, separating shock and shock precursor components (Villar-Martín et al. 1999).

It is possible to make successful double-Gaussian fits to the [O III] λ5007 line across the full spatial extent over which the line is detected in Cygnus A, providing information about the linewidths, shifts and flux profile. However, in the far SE region, only single-Gaussian fits are used, since the addition of a second Gaussian made

Table 1. A full list of observed emission-line widths for each aperture.

Line ID	Width (km s^{-1}) A	B	C	D
[O II] λ3727	480 ± 4	415 ± 4	374 ± 4	340 ± 4
[Ne III] λ3869	441 ± 7	357 ± 7	259 ± 4	220 ± 5
H8 + He I	460 ± 52	365 ± 72	292 ± 57	269 ± 72
[Ne III] λ3889	467 ± 12	461 ± 17	359 ± 13	323 ± 18
[S II] λ4069	484 ± 63	358 ± 30	206 ± 25	–
[S II] λ4076	483 ± 63	357 ± 31	206 ± 25	–
Hδ	373 ± 21	349 ± 26	257 ± 20	190 ± 16
Hγ	485 ± 12	380 ± 10	309 ± 9	273 ± 11
[O III] λ4363	492 ± 25	421 ± 24	285 ± 18	256 ± 23
He II λ4686	504 ± 15	449 ± 20	320 ± 12	276 ± 10
[Ar IV] λ4711	554 ± 72	377 ± 86	129 ± 25	297 ± 66
[Ar IV] λ4740	551 ± 72	238 ± 86	487 ± 91	313 ± 44
Hβ	458 ± 7	394 ± 6	309 ± 5	266 ± 5
[O III] λ4959	479 ± 7	453 ± 6	307 ± 3	245 ± 2
[O III] λ5007	474 ± 7	448 ± 6	304 ± 3	243 ± 2
[N II] λ5754	379 ± 28	424 ± 30	450 ± 41	475 ± 46
He I λ5876	429 ± 36	457 ± 21	362 ± 26	166 ± 26
[Fe VII] λ6086	776 ± 59	847 ± 45	680 ± 47	358 ± 29
[O I] λ6300	445 ± 12	443 ± 3	407 ± 8	257 ± 6
[SIII] λ6312	222 ± 56	501 ± 37	484 ± 144	235 ± 54
[O I] λ6363	471 ± 30	442 ± 9	432 ± 20	304 ± 21
[Fe X] λ6374	144 ± 169	894 ± 148	766 ± 130	460 ± 125
[Ar V] λ6435	550 ± 210	246 ± 54	319 ± 66	131 ± 28
[N II] λ6548	376 ± 13	462 ± 6	421 ± 3	254 ± 3
Hα	616 ± 46	494 ± 10	429 ± 5	289 ± 6
[N II] λ6548	374 ± 13	460 ± 6	419 ± 3	253 ± 3
[S II] λ6717	397 ± 7	441 ± 3	422 ± 3	285 ± 3
[S II] λ6731	396 ± 7	440 ± 3	422 ± 3	284 ± 3
[Ar V] λ7005	722 ± 125	703 ± 108	519 ± 101	264 ± 59
He I λ7065	204 ± 64	529 ± 88	639 ± 220	319 ± 88
[Ar III] λ7136	404 ± 37	509 ± 12	441 ± 10	293 ± 8

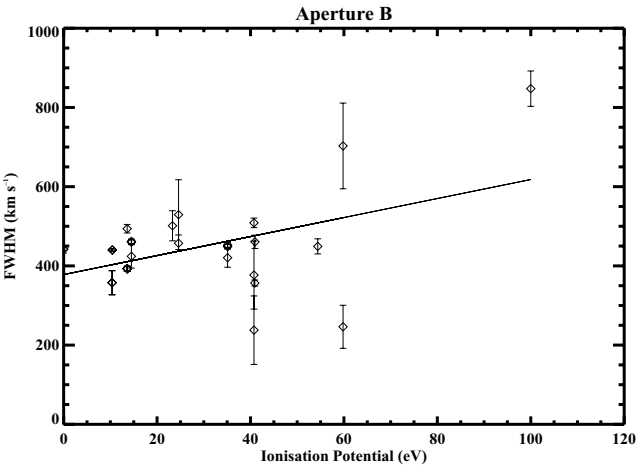

Figure 4. Plot of the ionization potential of the emission lines against instrumentally corrected FWHM for the nuclear aperture. The values of the ionization potential were obtained from de Robertis & Osterbrock (1984).

no improvement to the fit. Double Gaussians were therefore fitted to the [O III] λλ4959, 5007 lines on a pixel-by-pixel basis, constraining the widths of the doublet lines to be equal and the intensity of the λ5007 line to be 2.985 times that of the λ4959 line, for each of the two kinematic subcomponents. It can be seen from Fig. 5 (middle column) that these double-Gaussian fits provide a better fit to the broad wings of the lines in the nuclear regions. The fluxes, instrumentally corrected linewidths and wavelength shifts for the two kinematic subcomponents are plotted against position in Figs 6, 7 and 8.

Fig. 6 shows the spatial variations in the [O III] λ5007 flux. In the central regions ($r < 1$ arcsec) the profile can be characterized by 'broad' (FWHM > 500 km s^{-1}) and 'narrow' (FWHM < 300 km s^{-1}) components; while in the outer regions the profile can be characterized by two 'narrow' components (FWHM < 500 km s^{-1}) of different width and/or radial velocity. Note that the peak flux in the broad component coincides with a minimum in the flux of the narrow component (see also Fig. 1).

Fig. 7 shows the spatial variation in the emission-line width (FWHM) for the [O III] λ5007 line. We see evidence for a broad (500–850 km s^{-1} FWHM) component across a significant spatial range of the galaxy, ±1 arcsec on the sky. The width and shift of the broad component vary with spatial position. If we fix the shift and width of the broad component to be the same as those of the nuclear pixel, the subsequent fits do not adequately model the profile of the emission line at other spatial positions. Therefore this broad component is spatially resolved.

Fig. 8 shows the shift of the broad and narrow components of each line compared to the laboratory wavelength. There is evidence of line splitting in both the NW and SE regions of the galaxy. By looking at Fig. 7 it can be seen that these are regions in which no broad components are fitted, implying that we are actually fitting the split components of these lines rather than broad and narrow ones.

3.3 Other line ratios

Following the detection of a broad component in the [O III] λλ4959, 5007 lines, the next step is to investigate whether this broad component exists in the other lines of the Cygnus A spectrum.

The information obtained from the double-Gaussian [O III] λλ5007, 4959 fits was used to constrain the input parameters for double-Gaussian fits to the other lines. This is similar to the approach used by Villar-Martín et al. (1999), who assumed that all the lines have the same number of components, with the same velocity width and velocity shifts as the [O III] line. Fig. 5 shows that, using these assumptions, the double-Gaussian fits for the Hβ and [O I] λ6300 lines in the nuclear aperture provide a good match to the line profiles. In aperture A (NW) the fits relate to the two components of the split line rather than a broad and a narrow component as is the case in apertures B and C. In aperture D, however, only single-Gaussian fits were used for the analysis, as fitting double Gaussians did not improve the fit to the emission lines.

3.3.1 Reddening

We expect Cygnus A to be reddened due to its location close to the Galactic plane, but previous low-resolution spectral studies also show evidence for significant reddening intrinsic to the host galaxy of Cygnus A (Tadhunter et al. 1994). To study the contributions of these effects, and to determine whether the broad and narrow components are reddened differently, we have examined the spatial variations of the Balmer line ratios.

The Balmer line ratios (Hα/Hβ, Hγ/Hβ, Hδ/Hβ) provide an estimate of the total reddening of each subcomponent in each aperture. Using the Seaton (1979) renormalization of the Nandy et al. (1975) extinction curve, with case B recombination line values from Gaskell

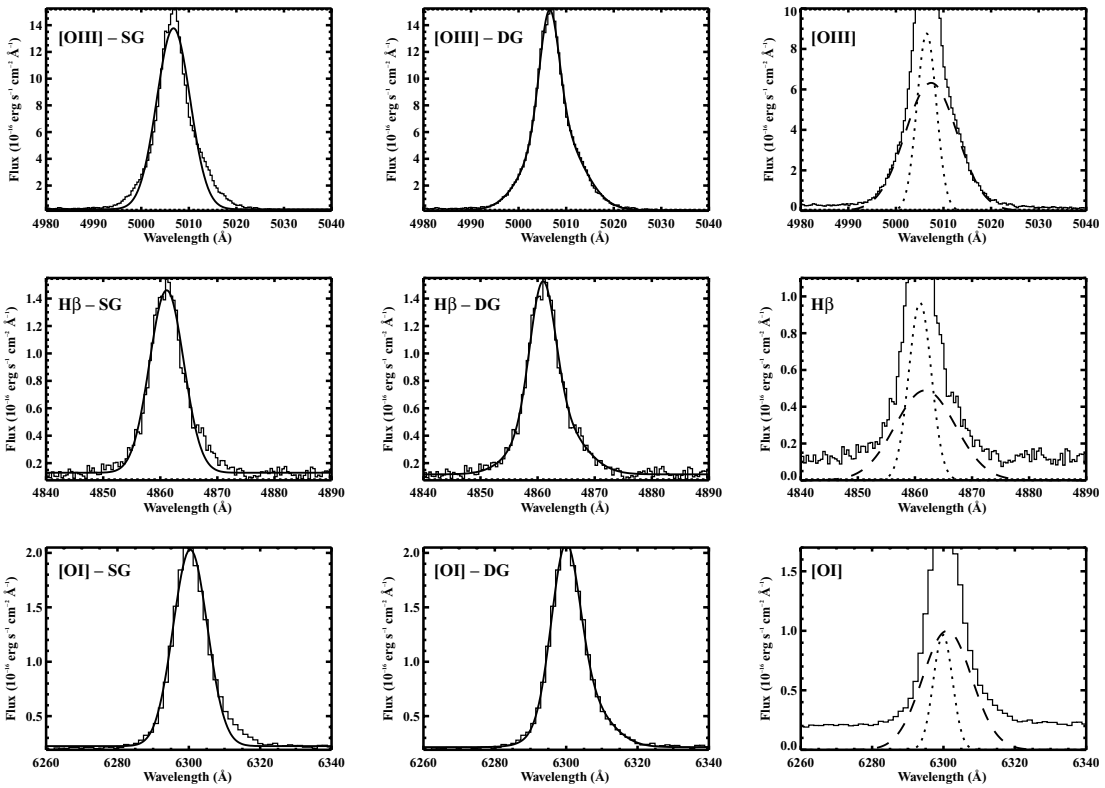

Figure 5. Gaussian fits to the [O III] λ5007 (top), Hβ (middle) and [O I] λ6300 (bottom) lines. The left-hand column shows the result of single-Gaussian (SG) fits – note that the broad wings are not adequately fitted. The middle column shows the result of double-Gaussian (DG) fits. The right-hand column shows the two components of these double-Gaussian fits, with the dotted lines representing the narrow components and the dashed lines the broad components.

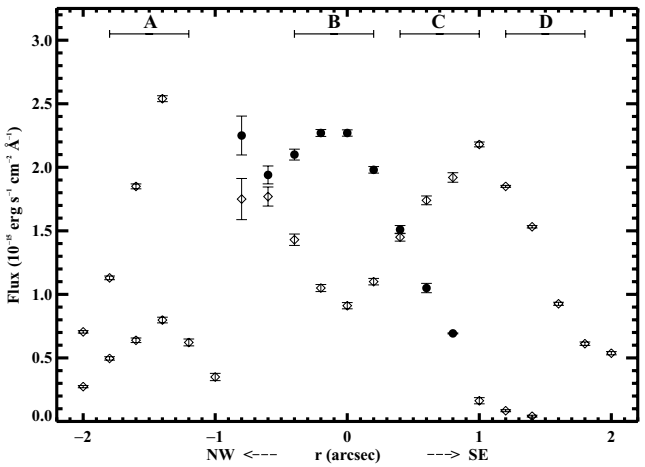

Figure 6. Spatial variations in the flux for the [O III] λ5007 line derived from the double-Gaussian fits. The open diamonds and the filled circles respectively represent the narrower and the broader components of the fit at each spatial location.

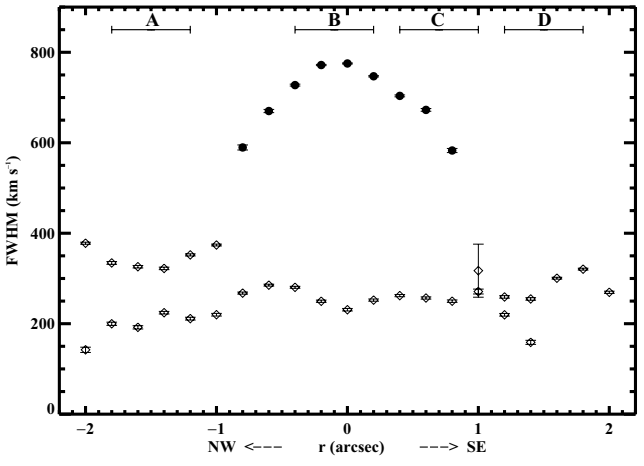

Figure 7. Spatial variations in the emission-line width (FWHM) for the [O III] λ5007 line. The open diamonds and the filled circles respectively represent the narrower and the broader components of the fit.

& Ferland (1984) for Hα/Hβ of 3.1,[1] and case B values from Osterbrock (1989) for the other line ratios, we obtain the estimates of $E(B-V)$ for the broad and narrow components shown in Table 2. The values obtained from Hδ/Hβ are discrepant when compared to the values for the other two line ratios, in the sense that they are systematically larger for most apertures and components. This is likely to be due to the effects of underlying Hδ line absorption associated with young stars (Fosbury et al., in preparation). However, the Hα/Hβ and Hγ/Hβ ratios give consistent results taking into account the uncertainties. Therefore, for the reddening-corrected line ratios listed in Table 3, we used the weighted mean of the results from the Hα/Hβ and Hγ/Hβ Balmer line pairs in order to correct for reddening.

[1] We use the value from Gaskell & Ferland (1984) for Hα/Hβ because this is more appropriate for AGN-photoionized gas, as it takes into account the collisional excitation and radiative transfer effects that may be present.

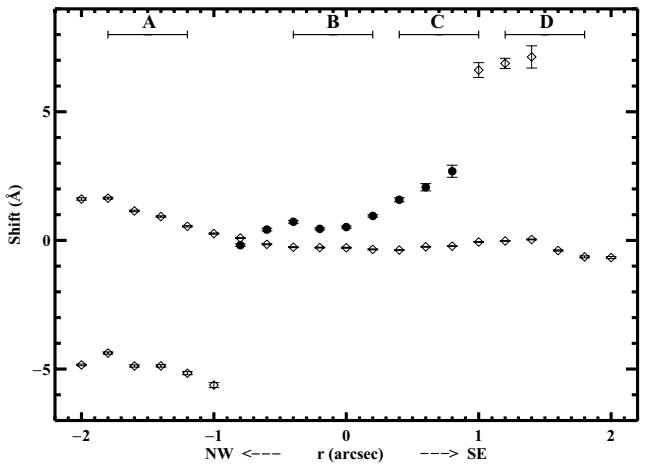

Figure 8. Plot showing the shifts of the [O III] λ5007 line centre compared to the actual value (5006.843 Å) for the broad and narrow components. The open diamonds and the filled circles respectively represent the narrower and the broader components of the fit.

Independent studies of the Galactic contribution to the reddening, using field galaxies close to Cygnus A, give $E(B-V) \sim 0.4$ (van den Bergh 1976; Spinrad & Stauffer 1982). The weighted mean results for apertures B (nuclear) and C suggest that the narrow component is reddened mainly by the Galaxy, whereas the broad component shows significant intrinsic reddening due to dust in the host galaxy of Cygnus A. However, in apertures A and D the $E(B-V)$ value suggests mainly Galactic reddening.

From this we conclude that, in the outer regions of Cygnus A ($r > 1$ arcsec), the reddening is largely due to our Galaxy; however, in the central regions there is significant intrinsic reddening. The majority of this reddening is associated with the broad component of the lines; on the basis of our data there is no evidence for intrinsic reddening in the narrow kinematic components in any of the spatial regions.

Comparing the $E(B-V)$ values calculated for the nuclear region with those calculated in Tadhunter et al. (1994), we find that the narrow component value is significantly lower than their value of ∼0.7, whereas the broad component has a significantly larger value. However, the average value of the broad and narrow components is consistent with that obtained by Tadhunter et al. (1994).

3.4 Ionization and physical conditions

The line ratios for the broad and narrow components shown in Table 3 were corrected for reddening using the mean values of $E(B-V)$ from Table 2. Following the reddening correction we find remarkable uniformity in the ionization-sensitive line ratios between the different spatial and kinematic subcomponents (see also the diagnostic diagrams in Section 4.3).

This uniformity is also apparent in the physical conditions. Using the standard spectral diagnostic techniques we have estimated the electron temperature (from the [N II] and [O III] lines) and density (from the [S II] lines) from the reddening-corrected broad- and narrow-line fluxes for each of the four apertures. These were calculated using the TEMDEN facility within NEBULAR (part of the STSDAS package of IRAF), which is based on the five-level atom calculator developed by de Robertis, Dufour & Hunt (1987). Given a nominal density and value of the temperature diagnostic line ratio, the package can be used to estimate the temperature of the line-emitting region, and vice versa. The results are shown in Table 4: n_e[S II] was calculated from the [S II] λ6717/6731 ratio assuming $T_e = 10^4$ K; T_e[N II] was calculated from the [N II] λ(6584 + 6548)/5755 ratio assuming $n_e = 300$ cm^{-3}; and T_e[O III] was calculated from the [O III] λ(5007 + 4959)/4363 ratio assuming $n_e = 300$ cm^{-3}.

We see from the table that the electron temperatures calculated from both the [N II] and [O III] lines, whilst differing between the two sets of diagnostic lines, *are similar in both the narrow and broad components of the fit for each aperture and show no significant variation across the four apertures*. The estimated temperatures are $T_e \sim 15\,000$ K using the [O III] diagnostic lines and $T_e \sim 10\,000$ K using the [N II] diagnostic lines.

The ratio of the [S II] lines, used to calculate the electron density, is shown as a function of position in Fig. 9. Taking into account the errors, we see that the ratio of these lines does not vary significantly across the apertures and subcomponents. Where accurately measured (i.e. 3σ from the low-density limit), the estimated electron densities fall in the range 180 to 380 cm^{-3}. This is consistent with previous studies (Tadhunter et al. 1994) and there is no evidence for high densities in any of the components.

3.4.1 *[Fe VII] and other high ionization lines*

Based on single-Gaussian fits (Table 1), the [Fe VII] λ6086 line appears to be particularly broad (FWHM ∼ 850 km s^{-1} in the nuclear aperture) compared with the other emission lines in three of the four apertures (excluding aperture D) of the galaxy. Fig. 10 shows the spectrum of this line for the four apertures with the Gaussian fit overplotted.

Using single-Gaussian fits we find that we can fit the [Fe X] λ6374 line as a wing of the [O I] λ6363 line. However, when double-Gaussian fits are used, these model the [O I] λ6363 line completely and we are unable to fit the [Fe X] line in the wing of the line. Therefore, it remains unclear whether [Fe X] is present in the spectrum of Cygnus A (see also Tadhunter et al. 1994).

Based on the single-Gaussian fits, the iron lines are broader than any of the other lines measured in the same aperture. However, it is notable that the width of the broad component fitted to the [O III]

Table 2. The $E(B-V)$ values obtained for each aperture, for each set of Balmer lines for the narrow and broad components. Also shown are the results of calculating the weighted mean of Hα/Hβ and Hγ/Hβ for each aperture – this is the value that was used for the reddening correction.

	Hα/Hβ		Hγ/Hβ		Hδ/Hβ		Weighted mean	
Aperture	N	B	N	B	N	B	N	B
A	0.48 ± 0.10	0.48 ± 0.03	0.26 ± 0.16	0.52 ± 0.05	1.65 ± 0.48	0.48 ± 0.07	0.46 ± 0.08	0.49 ± 0.02
B	0.43 ± 0.05	0.81 ± 0.05	0.43 ± 0.11	0.98 ± 0.15	0.74 ± 0.15	1.37 ± 0.29	0.45 ± 0.04	0.84 ± 0.05
C	0.33 ± 0.07	0.97 ± 0.10	0.65 ± 0.12	0.85 ± 0.36	0.62 ± 0.16	1.36 ± 0.62	0.43 ± 0.05	0.97 ± 0.10
D	0.48 ± 0.02		0.45 ± 0.09		0.81 ± 0.13		0.48 ± 0.02	

Table 3. List of the reddening-corrected line flux ratios for the broad and narrow components of each line relative to Hβ for each of the four apertures. The lines have been fitted using the same model, after taking into account instrumental broadening and the wavelength dependence of velocity, as the [O III] λ5007 line (see Section 3.3). The columns show (1) the probable line ID and then for each aperture (2) the ratio of the narrow line relative to Hβ and (3) the ratio of the broad line relative to Hβ. The Hβ flux, both observed and reddening-corrected, is shown in units of 10^{-16} erg s^{-1} cm^{-2} Å^{-1}.

Line	A		B		C		D
ID	C1 ratio	C2 ratio	N ratio	B ratio	N ratio	B ratio	Ratio
[O II] λ3727	1.91 ± 0.20	4.96 ± 0.13	3.59 ± 0.24	2.44 ± 0.43	3.54 ± 0.16	2.89 ± 0.73	3.56 ± 0.23
[Ne III] λ3869	1.32 ± 0.06	1.22 ± 0.02	0.94 ± 0.03	0.81 ± 0.05	1.09 ± 0.04	0.58 ± 0.11	1.11 ± 0.03
H8 + He I	0.21 ± 0.05	0.14 ± 0.01	0.10 ± 0.03	0.16 ± 0.04	0.11 ± 0.03	0.19 ± 0.09	0.11 ± 0.02
[Ne III] λ3889	0.55 ± 0.06	0.50 ± 0.02	0.29 ± 0.02	0.52 ± 0.04	0.32 ± 0.02	0.67 ± 0.09	0.44 ± 0.02
[S II] λ4069	0.13 ± 0.01	0.13 ± 0.01	0.17 ± 0.03	–	0.13 ± 0.03	0.05 ± 0.07	–
[S II] λ4076	0.04 ± 0.04	0.04 ± 0.01	0.09 ± 0.01	–	0.06 ± 0.02	–	–
Hδ	0.12 ± 0.03	0.25 ± 0.01	0.20 ± 0.02	0.17 ± 0.03	0.22 ± 0.02	0.19 ± 0.07	0.20 ± 0.02
Hγ	0.51 ± 0.04	0.46 ± 0.01	0.47 ± 0.02	0.44 ± 0.03	0.42 ± 0.02	0.49 ± 0.07	0.47 ± 0.02
[O III] λ4363	0.25 ± 0.03	0.22 ± 0.01	0.17 ± 0.03	0.23 ± 0.02	0.23 ± 0.02	0.20 ± 0.07	0.25 ± 0.02
He II λ4686	0.66 ± 0.05	0.22 ± 0.01	0.20 ± 0.02	0.29 ± 0.02	0.30 ± 0.02	0.34 ± 0.06	0.41 ± 0.02
[Ar IV] λ4711	0.10 ± 0.03	0.08 ± 0.01	0.05 ± 0.02	0.07 ± 0.02	0.30 ± 0.01	–	0.09 ± 0.02
[Ar IV] λ4740	0.09 ± 0.03	0.05 ± 0.01	0.04 ± 0.03	0.04 ± 0.03	0.03 ± 0.02	0.15 ± 0.05	0.12 ± 0.01
Hβ	1.00 ± 0.04	1.00 ± 0.01	1.00 ± 0.03	1.00 ± 0.04	1.00 ± 0.03	1.00 ± 0.07	1.00 ± 0.02
[O III] λ4959	4.54 ± 0.18	3.87 ± 0.05	3.01 ± 0.09	4.18 ± 0.12	4.33 ± 0.10	3.84 ± 0.24	4.15 ± 0.07
[O III] λ5007	13.39 ± 0.53	11.41 ± 0.13	8.81 ± 0.26	12.07 ± 0.35	12.72 ± 0.31	11.03 ± 0.68	12.19 ± 0.20
[N II] λ5754	0.10 ± 0.02	0.11 ± 0.01	0.09 ± 0.02	0.08 ± 0.01	0.04 ± 0.01	0.12 ± 0.02	0.06 ± 0.01
He I λ5876	0.14 ± 0.02	0.12 ± 0.01	0.13 ± 0.02	0.12 ± 0.01	0.12 ± 0.02	0.08 ± 0.03	0.07 ± 0.01
[Fe VII] λ6086	0.16 ± 0.02	0.07 ± 0.01	–	0.17 ± 0.01	0.02 ± 0.01	0.24 ± 0.02	0.15 ± 0.01
[O I] λ6300	0.80 ± 0.05	1.00 ± 0.02	0.95 ± 0.04	1.12 ± 0.04	0.65 ± 0.04	1.29 ± 0.08	0.69 ± 0.02
[O I] λ6363	0.29 ± 0.05	0.33 ± 0.02	0.31 ± 0.01	0.37 ± 0.01	0.22 ± 0.01	0.42 ± 0.03	0.26 ± 0.02
[N II] λ6548	1.63 ± 0.12	2.02 ± 0.04	2.26 ± 0.08	2.30 ± 0.08	1.54 ± 0.08	2.56 ± 0.17	1.77 ± 0.03
Hα	3.40 ± 0.42	3.30 ± 0.11	3.41 ± 0.22	3.25 ± 0.20	3.03 ± 0.25	3.33 ± 0.43	3.09 ± 0.07
[N II] λ6548	4.75 ± 0.34	6.03 ± 0.11	6.76 ± 0.23	6.82 ± 0.23	4.62 ± 0.23	7.56 ± 0.50	5.27 ± 0.09
[S II] λ6717	3.92 ± 0.15	1.17 ± 0.03	2.05 ± 0.09	2.18 ± 0.11	1.38 ± 0.08	2.38 ± 0.25	1.65 ± 0.03
[S II] λ6731	3.58 ± 0.14	1.05 ± 0.03	1.62 ± 0.09	1.87 ± 0.12	0.88 ± 0.06	2.49 ± 0.23	1.32 ± 0.03
[Ar V] λ7005	0.08 ± 0.01	0.03 ± 0.01	0.02 ± 0.01	0.04 ± 0.01	0.03 ± 0.01	0.05 ± 0.01	0.04 ± 0.01
He I λ7065	–	0.06 ± 0.01	0.03 ± 0.01	0.03 ± 0.01	–	–	0.04 ± 0.01
[Ar III] λ7136	0.25 ± 0.03	0.26 ± 0.01	0.29 ± 0.02	0.39 ± 0.02	0.23 ± 0.02	0.48 ± 0.04	0.36 ± 0.01
Hβ flux (obs.)	1.81 ± 0.05	7.30 ± 0.05	4.81 ± 0.10	6.49 ± 0.18	5.31 ± 0.10	2.97 ± 0.16	4.36 ± 0.06
Hβ flux (cor.)	2.23 ± 0.06	9.98 ± 0.07	5.72 ± 0.12	29.94 ± 1.30	5.87 ± 0.12	21.51 ± 1.16	5.75 ± 0.08

Table 4. The temperature for the four apertures in the narrow and broad components calculated using standard spectroscopic techniques. The values used have been corrected for reddening.

	T_e[N II] (K)		T_e[O III] (K)	
Aperture	N	B	N	B
A	$11\,900^{+1100}_{-800}$	$11\,100^{+200}_{-200}$	$14\,900^{+1000}_{-800}$	$14\,900^{+300}_{-300}$
B	$10\,100^{+800}_{-600}$	$9\,000^{+800}_{-600}$	$15\,100^{+800}_{-700}$	$15\,000^{+800}_{-700}$
C	$8\,200^{+1500}_{-800}$	$10\,600^{+1200}_{-800}$	$14\,600^{+700}_{-600}$	$14\,400^{+3500}_{-1700}$
D	$8\,900^{+500}_{-400}$		$15\,500^{+600}_{-500}$	

λ5007 line is consistent with the width of the [Fe VII] lines within the errors. We further note that the [Fe VII] and [Ar V] λ7005 lines appear to be correlated: both are dominated by broad components in the central regions, with no significant detection of a narrow component.

It has been suggested (e.g. Penston et al. 1984; Ferguson, Korista & Ferland 1997) that the lines from the highly ionized species of iron detected in Seyfert galaxies originate from a region intermediate between the conventional broad- and narrow-line regions, thus explaining the larger width of these lines compared to other forbidden emission lines. However, in this case we would expect to detect the [Fe VII] lines only in the nuclear region, and not in the more spatially extended regions. Therefore, our observations provide no support for the idea that these high ionization lines are associated solely with an unresolved INLR.

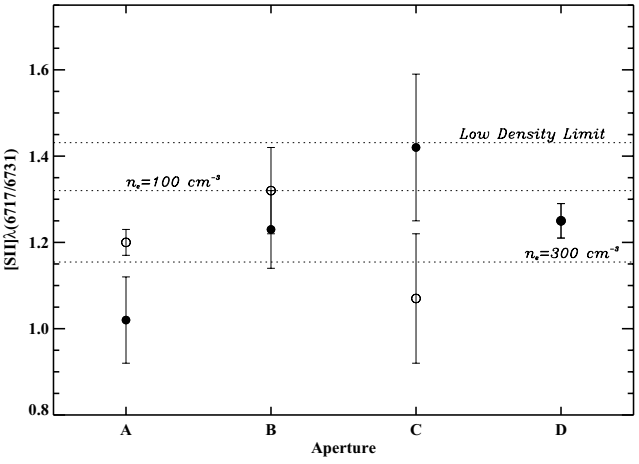

Figure 9. Plot showing the spatial variation of the [S II] λ6717/6731 ratio across the four apertures. The open circles and the filled circles respectively represent the narrower and the broader components of the fit.

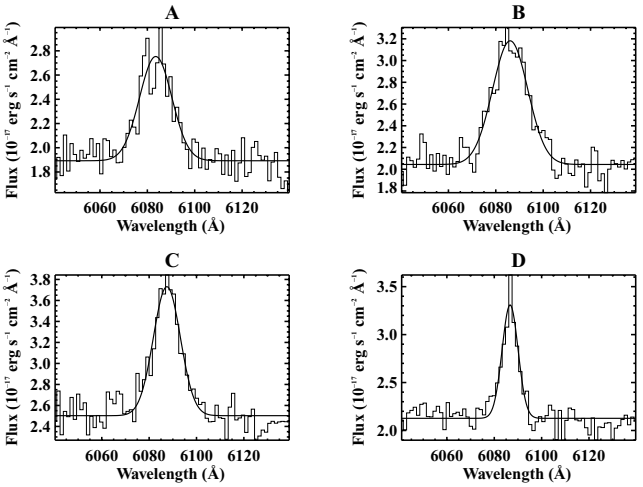

Figure 10. Plots showing the broad [Fe VII] λ6086 line for each aperture overplotted with a single-Gaussian fit. The broad component in the nuclear region (aperture B) is ∼850 km s^{-1} (FWHM).

3.5 Summary of results

The key results from this study can be summarized as follows:

(i) **Complexity.** We observe complex forbidden-line profiles with a spatially extended broad component (FWHM > 500 km s^{-1}) detected up to 1 kpc from the core. There is also evidence for emission-line splitting in both the NW and SE regions of the galaxy.

(ii) **Uniformity.** Despite the complex emission-line profiles, there is a remarkable uniformity in the ionization-sensitive line ratios and the physical conditions across all spatial regions. A similar uniformity in emission-line properties has been deduced from low-resolution long-slit spectra of the powerful radio galaxy 3C 321 (Robinson et al. 2000). The fact that this uniformity is observed across *all* kinematic subcomponents, and not just the different spatial regions, makes it all the more remarkable.

(iii) **Reddening.** We find no evidence for intrinsic reddening over and above the Galactic value, apart from in the broad component of the near-nuclear regions, which appears to be highly reddened ($A_{\mathrm{H}\beta} \simeq 1.8$ above Galactic).

(iv) **High ionization lines.** We find spatially extended [Fe VII] and [Ar V] lines that are associated wholly with the broad component in the near-nuclear regions.

We now consider the implications of these results for models of the NLR.

4 DISCUSSION

4.1 The structure of the NLR

Using the data presented in this paper we are now in a position to map out the structure of the NLR in Cygnus A.

We observe a broad component (FWHM > 500 km s^{-1}) in the near-nuclear region (up to 1 kpc from the core of the galaxy). This broad component is highly reddened [$E(B-V) \sim 0.9$, ∼0.5 mag above the Galactic value] and is therefore likely to originate deep in the central dust lane of Cygnus A. The location of the broad component in the nucleus coincides with the high surface brightness 'V'-shaped core emission-line structure seen in *HST* images of Cygnus A (Jackson et al. 1998). Comparing the spatially integrated spectra of this region obtained using the STIS spectrograph on *HST* (Tadhunter et al. 2003) with the data presented in this paper, we find that they both give the same result for the linewidth (FWHM ∼ 800 km s^{-1}) and redshift ($z = 0.056\,045$) of the nuclear broad component.

The narrow component in the near-nuclear regions is found to be reddened almost entirely by our Galaxy and shows little evidence for any intrinsic reddening. This suggests that the near-nuclear narrow component originates from a region in the foreground of the galaxy – away from the central dust lane – most likely the edge of the illumination cone closest to the observer.

In the more spatially extended regions ($r > 1$ arcsec) we find evidence for two narrow components. On this scale to both the NW and SE the brightest narrow component has a wavelength close to the expected rest value, whereas the fainter narrow component is shifted by 5–7 Å (280–400 km s^{-1}) relative to the rest wavelength, blueshifted in the case of the NW, but redshifted in the case of the SE. If the high-velocity components are a consequence of outflows, these results imply that the NW cone is in the foreground of the dust lane and the SE cone is in the background. This is also consistent with the high reddening measured in the region C and the results of Fosbury et al. (in preparation).

4.2 Is there an INLR?

The detection of a broad, highly reddened component in the nuclear regions may, on cursory inspection, appear consistent with the presence of an inner narrow-line region (INLR). However, upon closer inspection, the evidence for an INLR appears to be weak:

(i) We see no evidence for the expected correlation between the FWHM of the emission lines and critical density/ionization potential (as observed in Seyfert galaxies).

(ii) The broad component (FWHM > 500 km s^{-1}) is spatially extended and can be observed up to 1 kpc from the core of the galaxy. Observations using the STIS spectrograph (Tadhunter et al. 2003) have also shown the nuclear broad component to be spatially extended over a scale of ∼300 pc. The FWHM of the nuclear broad component measured from the spatially integrated STIS data is consistent the FWHM measured from the data presented in this paper.

(iii) There is no evidence for any unusual physical conditions (e.g. high densities).

In the frame of the unified schemes for powerful radio galaxies, the failure to detect an INLR is consistent with the status of Cygnus A as a narrow-line radio galaxy (NLRG) in which the quasar nucleus is not observed directly at optical wavelengths; if the INLR exists in this object, it must be compact enough to be hidden along our line of sight by the circumnuclear torus.

Note, however, that if we correct the flux of the broad component for reddening ($A_{\mathrm{H}\beta} \simeq 1.8$), it becomes the strongest emission-line component in the nuclear regions. Assuming that all the regions emitting the broad component appear unextinguished from the direction of the radio axis, the flux from the broad components would be ∼5 times brighter, and the total emission-line flux ∼2 times larger than measured along our line of sight. Thus the reddening associated with the kiloparsec-scale dust lane in Cygnus A can induce a mild (∼ factor 2) anisotropy in the emission-line flux from the nuclear regions. However, owing to the fact that only half (the near cone) of the region emitting the broad component may, in fact, be visible from the direction of the radio axis, and the other half blocked off by the dust lane or circumnuclear torus, this may overestimate the true level of anisotropy. Therefore, the anisotropy associated with the kiloparsec-scale dust lane is unlikely to be the sole factor

producing the observed differences between the [O III] emission-line luminosities of quasars and radio galaxies (Jackson & Browne 1991).

4.3 The ionization of the NLR

In order to determine the dominant ionization mechanism(s) for the NLR in Cygnus A, we have plotted diagnostic diagrams for various line ratio pairs. The Cygnus A line ratios are plotted together with data from literature for other NLRGs, including both NLR and EELR spectra, in Figs 11, 12 and 13.

The data are compared to three sets of photoionization models: power-law optically thick, blackbody optically thick, and mixed medium. The power-law model, $f_\nu \propto \nu^{\alpha_\nu}$, was calculated using the MAPPINGS photoionization code of Binette et al. (1997) using solar abundances and an optically thick, single slab photoionization model. Two power-law sequences are plotted, one with α_ν fixed at -1.5 and $10^{-4} < U < 0.1$, and the second with U fixed at 0.01 and $-2 < \alpha_\nu < -1$. The $\alpha_\nu = -1.5$ power-law continuum has been shown to give good fits to the stronger emission lines in low-redshift radio galaxies (Ferland & Osterbrock 1986; Robinson et al. 1987). Two different sets of blackbody models are also plotted with a range of temperatures and ionization parameters. In one set, the blackbody temperature is fixed at $T_\mathrm{b} = 160\,000$ K with the ionization parameter allowed to vary over the range $10^{-4} < U < 0.1$; whilst, in the other set, U was fixed at 10^{-2} and the temperature allowed to vary over the range $60\,000 < T_\mathrm{b} < 200\,000$ K. The mixed medium model includes a combination of optically thick and thin clouds and was developed by Binette, Wilson & Storchi-Bergmann (1996) in order to explain the discrepant high-ionization line ratios and high electron temperatures measured in many active galaxies. This model is shown as a sequence of $A_{M/I}$, the ratio of the solid angle covered by the optically thin component compared to that covered by the optically thick component. We plot two mixed medium models. The first sequence covers the range $0.04 < A_{M/I} < 116$ and was generated using tabulated values from Binette et al. (1996) for an illuminating power law with $\alpha_\nu = -1.3$ and a density of $n_0 = 50$ cm^{-3}. The second sequence is taken from (Binette et al. 1997, model M); it covers the same range of $A_{M/I}$ but using higher-density clouds ($n_0 = 1000$ cm^{-3}). The main advantage of the latter model for our purposes is that it includes the [Fe VII] λ6086 line.

Looking at the diagnostic diagrams for [O III] λ5007/Hβ versus [O II] λ3727/[O III] λ5007 and [O I] λ6300/[O III] λ5007 (Fig. 11), we see that the ratios for Cygnus A all fall in regions dominated by nuclear NLR for radio galaxies. The points for Cygnus A fit photoionization models for power-law or blackbody ionizing continua best, intercepting the models with values of U in the order $10^{-3} < U < 10^{-2}$. In the case of the [O III] λ5007/Hβ versus [O II] λ3727/[O III] λ5007 ratio, the points also fit both mixed medium models with intercepts in the range $1.6 < A_{M/I} < 4.0$. Closer inspection of the [O III] λ5007/Hβ versus [O I] λ6300/[O III] λ5007 plot shows that, although the points do not fit the mixed medium model as well, they project on to the same position along the $A_{M/I}$ sequence.

The diagnostic plot for [O III] λ5007/Hβ against [N II] λ6583/Hα (Fig. 12a) shows that all the models underpredict the ratio of the [N II] λ6583 (FWHM $\sim$ 800 km s^{-1}) for all components in Cygnus A. This issue was discussed by Tadhunter et al. (1994) who concluded that, provided the N/O abundance ratio is significantly enhanced with respect to the solar value, a combination of continuum energy distribution and cloud column density can be found that will provide agreement with the observed values for the required range in ionization parameter. Although they are plotted for solar N/O abundances, similar comments apply to the mixed medium models.

On the diagram of [O III] $\lambda(4959 + 5007)/4363$ against He II λ4686/Hβ (Fig. 12b), the Cygnus A points fall, as is the case with the previous plots, in the region dominated by nuclear NLR of radio galaxies. The points fit the mixed medium models best, intercepting the line at values $1.0 < A_{M/I} < 4.0$, which is consistent with the points found from the previous diagnostic plots. As noted by Tadhunter et al. (1989) the optically thick power-law and blackbody photoionization models can only fit the measured [O III] $\lambda(4959 + 5007)/4363$ in this and other radio galaxies for extremely high values of ionization parameter. However, such large ionization parameters are inconsistent with the position of the points relative to these models on other diagnostic diagrams (e.g. Fig. 11).

This is reinforced by the [O III] versus [N II] temperature diagnostic ratio plot shown in Fig. 13(a). Despite the fact that the optically thick photoionization models can produce the measured range in the [N II] ratio, the optical thick models struggle to reproduce the large [O III] λ4363/λ5007 ratios, even at high ionization parameters. Again the mixed medium models provide a better fit. The $A_{M/I}$ sequences for both of mixed medium models are compact on this diagram, but the $A_{M/I}$ values of intercept with the data are consistent with those found in the other diagnostic plots. These findings agree with Wilson, Binette & Storchi-Bergmann (1997), who suggested that a mixed medium model is required to explain the differences between the [O III] and [N II] electron temperatures, with the [O III] originating from the hot zone in matter-bounded clouds, and the [N II] from the cooler, partially ionized zones in the ionization-bounded clouds.

The [O III] λ5007/Hβ versus [Fe VII] λ6086/Hβ diagnostic plot shows that the points lie at the high ionization parameter end of the optically thick power-law and blackbody photoionization models – again, inconsistent with other diagnostic diagrams – and are slightly overpredicted by the high-density mixed medium model, although the points project on to the same range of $2.5 < A_{M/I} < 6.0$ as in the other diagnostic diagrams. Note, however, that the mixed medium models assume that the iron abundance is solar, and that the iron has not been depleted on to the dust grains; the agreement between the points and the mixed medium models could be improved by allowing for some depletion of the iron on to dust grains.

Although not presented here, we have also compared the line ratios for Cygnus A with pure shock and shock plus precursor models from Dopita & Sutherland (1996). These shock models do not provide as good a fit to the individual points and there is also less consistency in the position of the points relative to the shock models from diagram to diagram compared to the photoionization models.

On the basis of the consistency of the position of the data points relative to the model sequences on the various diagnostic diagrams, only the mixed medium photoionization models (with $1.6 < A_{M/I} < 4.0$) can provide an adequate fit to the line ratios measured in the various subcomponents of Cygnus A. The remaining small discrepancies between the models and the data could be resolved by fine-tuning the parameters of the mixed medium models (e.g. the relative element abundances). The identification of photoionization as the dominant ionization mechanism is consistent with the independent evidence for quasar illumination provided by the detection of ionization cones (Jackson et al. 1998) and a reflection nebulosity (Tadhunter et al. 1990; Ogle et al. 1997). We further note that *the general uniformity in the emission-line ratios and physical conditions between the various spatial and kinematical subcomponents suggests that the dominant ionization mechanism is the same for all subcomponents, and that the acceleration*

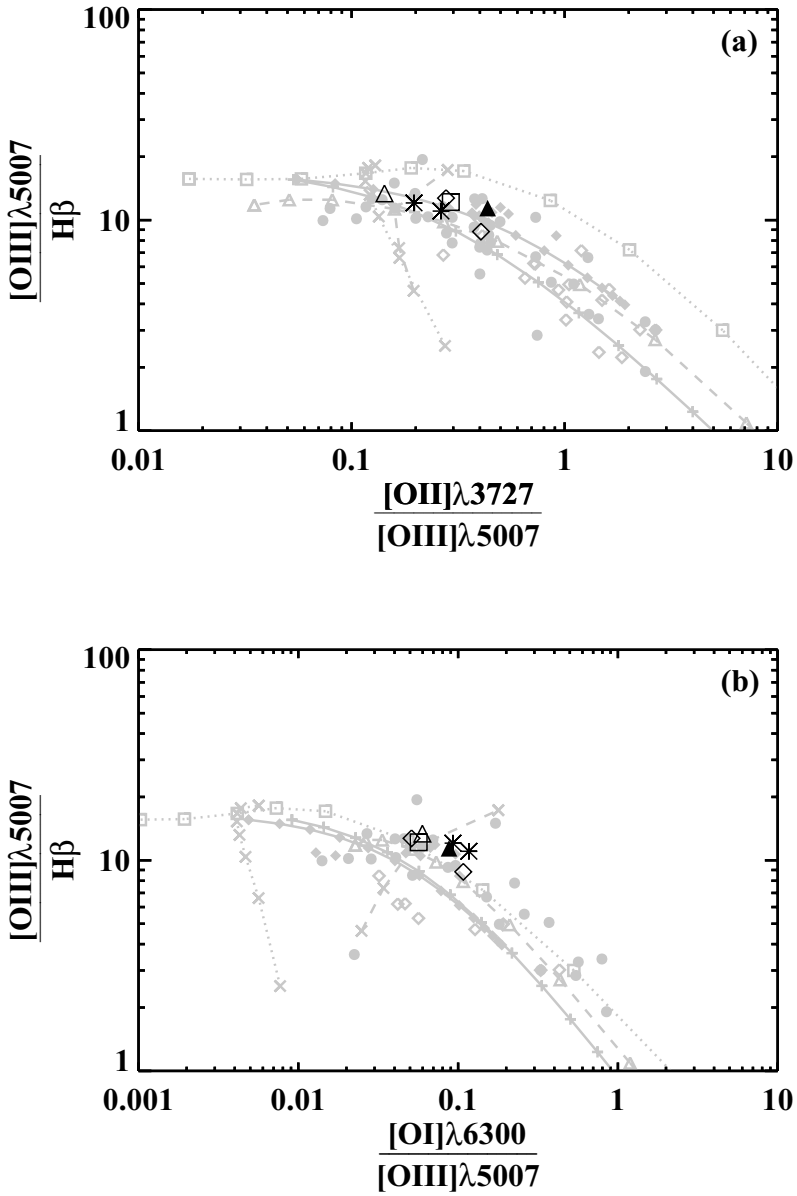

Figure 11. Diagnostic plots using the reddening-corrected line ratios of (a) [O III] λ5007/Hβ against [O II] λ3727/[O III] λ5007 and (b) [O I] λ6300/[O III] λ5007 respectively. The nuclear broad components (apertures B/C) of Cygnus A are represented by black stars, the nuclear narrow components by open diamonds, the SE single component by an open square, the 'narrow' NW component by an open triangle, and the 'broad' NW component by a filled triangle. Dashed lines represent power-law ionizing continua, $f \propto \nu^{\alpha_\nu}$, with triangles representing $\alpha_\nu = -1.5$, $U = 10^{-4}$, 2.5×10^{-4}, 5×10^{-4}, 10^{-3}, 2.5×10^{-3}, 5×10^{-3}, 0.01, 0.025, 0.05, 0.1, and crosses (×) showing models with U fixed at 0.01 and $\alpha_\nu = -2.00, -1.75, -1.50, -1.0$. Dotted lines are blackbody models, with squares representing sequences of models with $T = 160\,000$ K and the same sequence in U as before, and crosses showing sequences with $U = 0.01$ and $T = (0.6, 0.8, 1.0, 1.2, 1.4, 1.6, 1.8, 2.0) \times 10^5$ K. Solid lines with diamonds correspond to models with $\alpha_\nu = -1.3$ power law illuminating a mixture of optically thick and thin clouds, $A_{M/I} = 10^x(-1.4 \rightarrow 1.2$ in 0.2 intervals) (Binette et al. 1996) whilst the solid lines with plus signs (+) indicate the same sequence with much higher-density clouds (model M – Binette et al. 1997a). Also shown are points taken from the literature (Costero & Osterbrock 1977; Grandi & Osterbrock 1978; Cohen & Osterbrock 1981; Tadhunter 1986; Morganti et al. 1991; Tadhunter et al. 1994; Clark 1996; Storchi-Bergmann et al. 1996; Dickson 1997; Villar-Martín et al. 1998; Solórzano-Iñarrea, Tadhunter & Axon 2001; Wills et al. 2002); the diamonds represent EELRs and the circles nuclear narrow-line regions. Open diamonds represent the EELR of objects where there is evidence for jet–cloud interactions.

mechanism for the gas is not directly linked to how it is currently ionized. This is in contrast to the situation found in some jet–cloud EELR candidates (Villar-Martín et al. 1999).

4.4 The physical state of the NLR gas in Cygnus A

Two outstanding questions remain:

(i) What is the origin of the matter-bounded gas component required by the mixed medium models?

(ii) How do we account for such a high level of uniformity in the ionization and physical conditions, across a range of kinematic components, in the case of mixed medium photoionization?

A possible solution to these questions could be provided by the work of Robinson, Tadhunter & Dyson (2002), who, from an

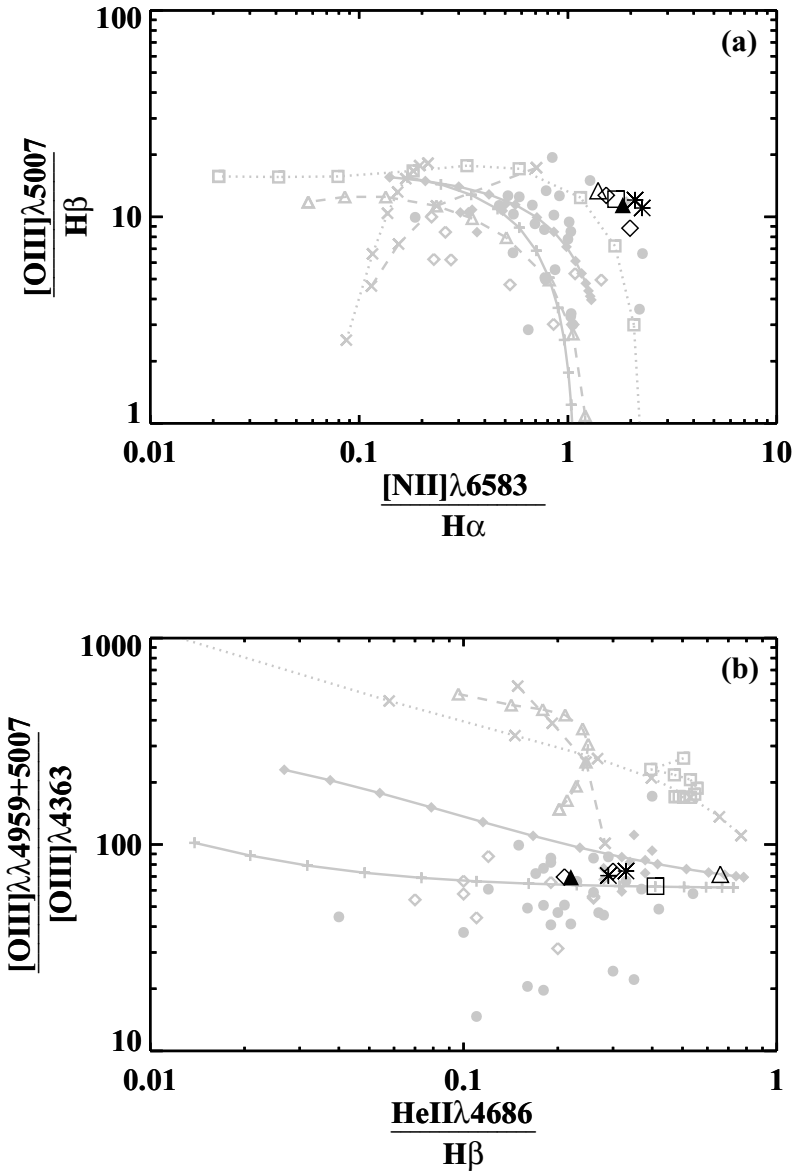

Figure 12. Diagnostic plots using the reddening-corrected line ratios of (a) [O III] λ5007/Hβ against [N II] λ6583/Hα and (b) [O III] λ(4959 + 5007)/[O III] λ4363 against [He II] λ4686/Hβ. The nuclear broad components (apertures B/C) of Cygnus A are represented by black stars, the nuclear narrow components by open diamonds, the SE single component by an open square, the 'narrow' NW component by an open triangle, and the 'broad' NW component by a filled triangle. The comparison models are the same as for Fig. 11.

analysis of the physical conditions of a number of radio galaxies, suggested that the line-emitting clouds may not yet have relaxed into pressure equilibrium following their initial photoionization by the AGN. Their model starts with cloud complexes that comprise cold, dense cloud cores, embedded in warm, lower-density outer shells. These in turn are in pressure equilibrium with a pervasive hot, low-density ISM. When the AGN switches on, the lower-density outer shells are instantaneously ionized, while an ionization front (IF) moves through the denser clumps. Immediately behind the IF, there is a high-density, overpressured region, and material expands away from this region until it is in pressure equilibrium with the hot ISM, at the same time becoming optically thin to the ionizing radiation. Subsequently, the ionizing radiation eats further into the dense clouds, always maintaining a high-density, high-pressure region immediately behind the IF and a low-density outer shell. This scenario provides a natural explanation for the mixed medium model (Binette et al. 1996) since, even if only a single, dense medium existed prior to photoionization, the expansion of material behind the ionization front would generate a low-density, optically thin halo. However, even allowing for the self-generation of the outer, matter-bounded component, it remains surprising that the correct mix of matter- and radiation-bounded components could be maintained for the range of kinematic subcomponents present in Cygnus A, given that these subcomponents may have had markedly different histories, and have been accelerated in different ways.

5 CONCLUSIONS

Our intermediate long-slit spectra of Cygnus A show considerable kinematic complexity in the near-nuclear regions of Cygnus A,

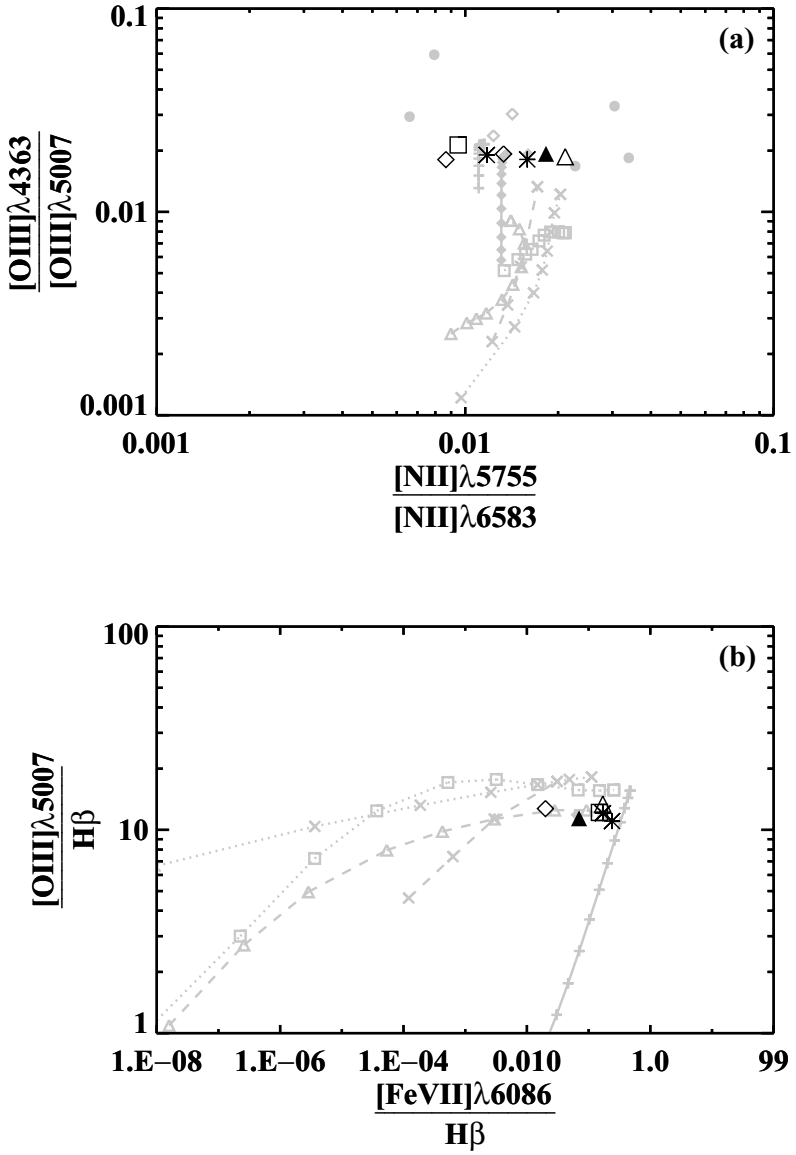

Figure 13. Diagnostic plots using the reddening-corrected line ratios of (a) [O III] λ4363/[O III] λ5007 against [N II] λ5755/[N II] λ6583 and (b) [O III] λ5007/Hβ against [Fe VII] λ6086/Hβ. The nuclear broad components (apertures B/C) of Cygnus A are represented by black stars, the nuclear narrow components by open diamonds, the SE single component by an open square, the 'narrow' NW component by an open triangle, and the 'broad' NW component by a filled triangle. The comparison models are the same as for Fig. 11.

coupled with a remarkable degree of uniformity in the ionization and physical conditions across the various spatial and kinematic subcomponents.

In detail we conclude the following:

(i) The dominant ionization mechanism for the warm gas sampled by our spectra is AGN photoionization of a mixed medium.

(ii) The ionization mechanism is the same for all the kinematic subcomponents, and the ionization of each subcomponent is not directly related to its acceleration.

(iii) The extinction effect of the kiloparsec-scale dust lane leads to a mild (at most $\sim$ factor 2) anisotropy in the emission-line flux, but we find no evidence for an INLR, consistent with the status of Cygnus A as an NLRG.

The main outstanding issues for the NLR in Cygnus A concern how the subcomponents are accelerated, and how the spectral uniformity is maintained across the range of spatial scales and kinematic components sampled in the near-nuclear regions.

ACKNOWLEDGMENTS

This paper is based on service observations made with the William Herschel Telescope, operated on the island of La Palma by the Isaac Newton Group in the Spanish Observatorio del Roque de los Muchachos of the Instituto de Astrofisica de Canarias. The authors acknowledge the data analysis facilities provided by the Starlink Project, which is run by CCLRC on behalf of PPARC. In addition, the following Starlink software packages have been used: FIGARO, KAPPA and DIPSO. MDT would like to thank TGR for his help and assistance with IDL and for a number of very useful plotting routines. MDT acknowledges a University of Sheffield Studentship. TGR acknowledges financial support from PPARC.

REFERENCES

Barthel P. D., 1989, ApJ, 336, 606
Binette L., Wilson A. S., Storchi-Bergmann T., 1996, A&A, 312, 365
Binette L., Wilson A. S., Raga A., Storchi-Bergmann T., 1997, A&A, 327, 909
Brotherton M. S., 1996, ApJS, 102, 1
Clark N. E., 1996, PhD thesis, Univ. Sheffield
Clark N. E., Axon D. J., Tadhunter C. N., Robinson A., O'Brien P., 1998, ApJ, 494, 546
Cohen R. D., Osterbrock D. E., 1981, ApJ, 243, 81
Costero R., Osterbrock D. E., 1977, ApJ, 211, 675
de Robertis M. M., Osterbrock D. E., 1984, ApJ, 286, 171
de Robertis M. M., Osterbrock D. E., 1986, ApJ, 301, 727
de Robertis M. M., Dufour R. J., Hunt R. W., 1987, J. R. Astron. Soc. Can., 81, 195
Dickson R. C., 1997, PhD thesis, Univ. Sheffield
Dopita M. A., Sutherland R. S., 1996, ApJS, 102, 161
Ferguson J. W., Korista K. T., Ferland G. J., 1997, ApJS, 110, 287
Ferland G. J., Osterbrock D. E., 1986, ApJ, 300, 658
Gaskell C. M., Ferland G. J., 1984, PASP, 96, 393
Grandi S. A., Osterbrock D. E., 1978, ApJ, 220, 783
Heckman T. M., Miley G. K., van Breugel W. J. M., Butcher H. R., 1981, ApJ, 247, 403
Heckman T. M., Miley G. K., Green R. F., 1984, ApJ, 281, 525
Hes R., Barthel P. D., Fosbury R. A. E., 1993, Nat, 362, 326
Jackson N., Browne I. W. A., 1990, Nat, 343, 43
Jackson N., Browne I. W. A., 1991, MNRAS, 250, 422
Jackson N., Tadhunter C., Sparks W. B., Miley G. K., Macchetto F., 1996, A&A, 307, L29
Jackson N., Tadhunter C., Sparks W. B., 1998, MNRAS, 301, 131
Morganti R., Robinson A., Fosbury R. A. E., Di Serego Alighieri S., Tadhunter C. N., Malin D. F., 1991, MNRAS, 249, 91
Nandy K., Thompson G. I., Jamar C., Monfils A., Wilson R., 1975, A&A, 44, 195
Ogle P. M., Cohen M. H., Miller J. S., Tran H. D., Fosbury R. A. E., Goodrich R. W., 1997, ApJ, 482, L37
Osterbrock D., 1989, Astrophysics of Gaseous Nebulae and Active Galactic Nuclei. University Science Books, Mill Valley, CA
Osterbrock D. E., Miller J. S., 1975, ApJ, 197, 535
Pelat D., Alloin D., Fosbury R. A. E., 1981, MNRAS, 195, 787
Penston M. V., Fosbury R. A. E., Boksenberg A., Ward M. J., Wilson A. S., 1984, MNRAS, 208, 347
Rawlings S., Saunders R., 1991, Nat, 349, 138
Robinson A., Binette L., Fosbury R. A. E., Tadhunter C. N., 1987, MNRAS, 227, 97
Robinson T. G., Tadhunter C. N., Axon D. J., Robinson A., 2000, MNRAS, 317, 922
Robinson T. G., Tadhunter C. N., Dyson J. E., 2002, MNRAS, 331, L13
Seaton M. J., 1979, MNRAS, 187, 73 P
Solórzano-Iñarrea C., Tadhunter C. N., Axon D. J., 2001, MNRAS, 323, 965
Spinrad H., Stauffer J. R., 1982, MNRAS, 200, 153
Stockton A., Ridgway S. E., Lilly S. J., 1994, AJ, 108, 414
Storchi-Bergmann T., Wilson A. S., Mulchaey J. S., Binette L., 1996, A&A, 312, 357
Tadhunter C. N., 1986, PhD thesis, Univ. Sussex
Tadhunter C. N., 1991, MNRAS, 251, 46 P
Tadhunter C. N., 2002, in Henney W. J., Steffen W., Raga A. C., Binette L., eds, Rev. Mex. Astron. Astrofis. Conf. Ser. Vol. 13, The Ionization of the Emission Line Gas in Nearby Powerful Radio Galaxies. Rev. Mex. Astron. Astrofis., p. 213
Tadhunter C. N., Robinson A., Morganti R., 1989, in Meurs E. J. A., Fosbury R. A. E., eds, Proc. ESO Workshop on Extranuclear Activity. European South. Obser., Garching bei Munchen, p. 293
Tadhunter C. N., Scarrott S. M., Rolph C. D., 1990, MNRAS, 246, 163
Tadhunter C. N., Metz S., Robinson A., 1994, MNRAS, 268, 989
Tadhunter C. N., Packham C., Axon D. J., Jackson N. J., Hough J. H., Robinson A., Young S., Sparks W., 1999, ApJ, 512, L91
Tadhunter C., Marconi A., Axon D., Wills K., Robinson T., Jackson N., 2003, MNRAS, in press
Thornton R. J., Stockton A., Ridgway S. E., 1999, AJ, 118, 1461
van den Bergh S., 1976, ApJ, 210, L63
Villar-Martín M., Tadhunter C., Morganti R., Clark N., Killeen N., Axon D., 1998, A&A, 332, 479
Villar-Martín M., Tadhunter C., Morganti R., Axon D., Koekemoer A., 1999, MNRAS, 307, 24
Whittle M., 1992, ApJ, 387, 121
Wills K. A., Tadhunter C. N., Robinson T. G., Morganti R., 2002, MNRAS, 333, 211
Wilson A. S., Binette L., Storchi-Bergmann T., 1997, ApJ, 482, L131

This paper has been typeset from a TEX/LATEX file prepared by the author.